

Cavity-driven Rabi oscillations between Rydberg states of atoms trapped on a superconducting atom chip

Manuel Kaiser^{1,*}, Conny Glaser^{1,†}, Li Yuan Ley¹, Jens Grimm¹, Helge Hattermann¹, Daniel Bothner^{1,‡}, Dieter Koelle¹, Reinhold Kleiner¹, David Petrosyan^{1,2}, Andreas Günther^{1,‡} and József Fortágh^{1,§}

¹*Center for Quantum Science, Physikalisches Institut, Eberhard Karls Universität Tübingen, Auf der Morgenstelle 14, D-72076 Tübingen, Germany*

²*Institute of Electronic Structure and Laser, FORTH, GR-70013 Heraklion, Crete, Greece*



(Received 21 October 2021; accepted 17 February 2022; published 18 March 2022)

Hybrid quantum systems involving cold atoms and microwave resonators can enable cavity-mediated infinite-range interactions between atomic spin systems and realize atomic quantum memories and transducers for microwave-to-optical conversion. To achieve strong coupling of atoms to on-chip microwave resonators, it was suggested to use atomic Rydberg states with strong electric-dipole transitions. Here we report on the experimental realization of coherent coupling of a Rydberg transition of ultracold atoms, trapped on an integrated superconducting atom chip, to the microwave field of an on-chip coplanar waveguide resonator. Close to the chip surface, stray electric fields lead to inhomogeneous Rydberg level shifts, which would hinder coherent interactions of atoms in a cloud with the Rydberg excitation lasers and the microwave cavity field. We, however, use optical excitation of a Rydberg state of atoms in a narrow layer with nearly constant electric field, which allows for resonant coupling of the atoms to the cavity microwave field on an appropriate Rydberg transition. We also achieve state-selective detection of the energetically close Rydberg states. We then observe and characterize cavity-driven Rabi oscillations between a pair of atomic Rydberg states. The residual damping of the oscillations is dominated by the spread of Rabi frequencies of atoms in different positions of the resonant cavity mode, as revealed by our model. Despite the technical challenges, our studies demonstrate the feasibility of coherent-state manipulation of Rydberg atoms interacting with superconducting circuits, paving the way for realization of capable hybrid quantum systems.

DOI: [10.1103/PhysRevResearch.4.013207](https://doi.org/10.1103/PhysRevResearch.4.013207)

I. INTRODUCTION

With the rise of quantum technologies, the development of hardware components for quantum simulation, information processing, storage and communication has acquired an unprecedented importance. To date, no single physical system is complete from a quantum engineer's perspective, i.e., universally suited to faithfully implement all necessary tasks. A promising route for resolving this problem is the construction of hybrid quantum systems [1–3], in which different physical components are combined on a single platform by interfacing fast quantum gates [4,5] with long-lived quantum memories [6,7] and optical quantum communication channels [8].

A particularly promising hybrid approach is to combine superconducting quantum circuits with ultracold atoms. Microwave cavities can strongly couple with superconducting

qubits [9] and mediate quantum state transfer between the qubits and spin ensemble quantum memories [10–12]. Cold atoms in magnetic microtraps possess excellent coherence properties [13–17] and strong optical (Raman) transitions and are therefore suitable systems to realize quantum memories and optical interfaces [18–22]. The hitherto achieved magnetic-dipole coupling between hyperfine states of trapped cold atoms and on-chip superconducting microwave resonators [23], is still too weak to implement truly quantum coherent operations. An advantageous alternative for enhancing the coupling is to employ appropriate atomic Rydberg transitions with strong electric-dipole moments [24–27].

Velocity-calibrated atoms prepared in circular Rydberg states and interacting one-by-one with a high- Q three-dimensional (3D) microwave cavity (photon box) constitute one of the most accurately controlled quantum optical systems [28]. Pioneering works have achieved electric-dipole coupling of Rydberg states of helium atoms in a supersonic beam with a coplanar microwave waveguide and a resonator [27,29]. On the other hand, long-lived coherence of Rydberg state superpositions of cold atoms above a superconducting chip have been demonstrated [16]. Hence, employing cold trapped atoms for a hybrid quantum system would greatly expand the functionality, flexibility, and controllability [25,26], and permit spatiotemporal control of interactions for the realization of on-demand quantum transducers [22,30,31].

*m.kaiser@uni-tuebingen.de

†conny.glaser@uni-tuebingen.de

‡a.guenther@uni-tuebingen.de

§fortagh@uni-tuebingen.de

Published by the American Physical Society under the terms of the [Creative Commons Attribution 4.0 International](https://creativecommons.org/licenses/by/4.0/) license. Further distribution of this work must maintain attribution to the author(s) and the published article's title, journal citation, and DOI.

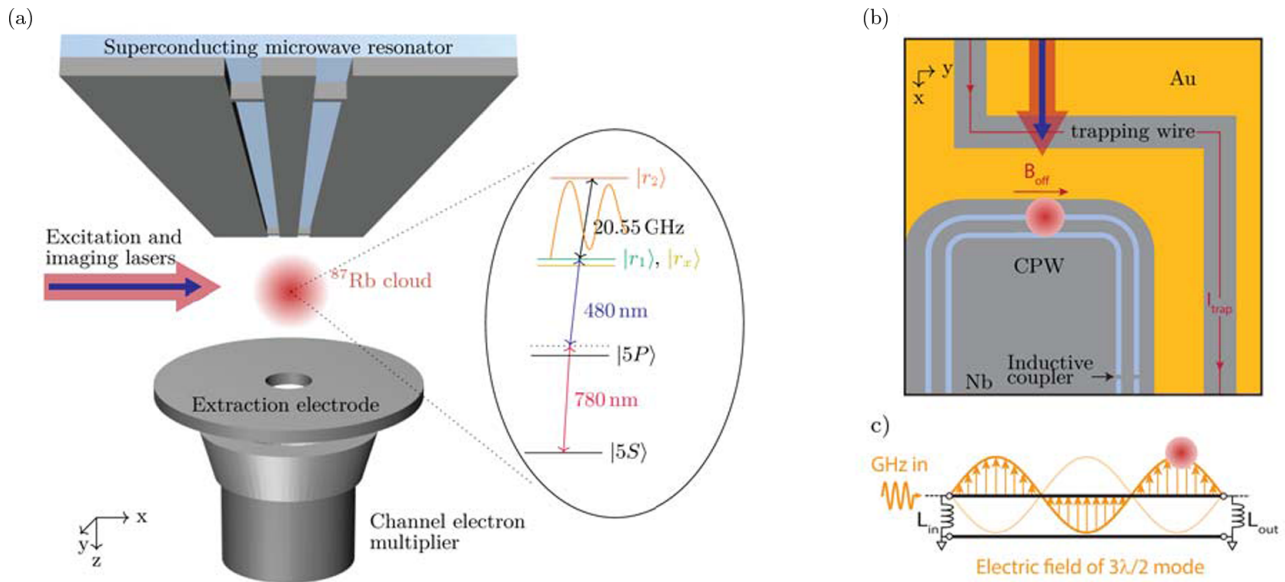


FIG. 1. Schematics of the experimental system (not to scale). (a) An ultracold cloud of ^{87}Rb atoms is trapped at $130\ \mu\text{m}$ distance from a CPW resonator. A pair of laser photons with wavelengths 780 and 480 nm excites the atoms from the ground state $|5S\rangle$ to a Rydberg state $|r_1\rangle$ (and $|r_x\rangle$) via an intermediate nonresonant state $|5P\rangle$. The microwave (MW) coplanar waveguide cavity (drawn as being straight in this schematic, on the actual chip it has a more complicated shape, cf. Ref. [23]) is coupled via a feedline to an external MW source. In turn, the electric field of the cavity drives the atomic transition from state $|r_1\rangle$ to another Rydberg state $|r_2\rangle$, inducing damped Rabi oscillations. An extraction electrode below the cloud is used to apply a DC electric field for Stark-tuning the Rydberg transition frequency, for field-ionization of Rydberg atoms, and for extraction of the ions from the atom cloud. The ions are detected with a channel electron multiplier and adjacent detection electronics. (b) Bottom view of the integrated superconducting atom chip containing a Z-shaped trapping wire and the CPW resonator: On a sapphire chip surface (blue), the trapping wire and the core of the MW resonator are made of superconducting niobium (gray), while parts of the ground plane are coated with normal conducting gold (yellow) to ensure a proper grounding of the CPW outer conductor [23,36]. The magnetic trap with an offset field B_{off} at the center is generated by the current I_{trap} running through the trapping wire, persistent supercurrents around the cavity gaps, and external magnetic fields from macroscopic wires and coils [37]. (c) Circuit scheme of the inductively coupled superconducting transmission line cavity and the corresponding standing-wave electric field of the third harmonic frequency $\omega_c = 2\pi \times 20.55\ \text{GHz}$. The atom cloud is trapped near one of the electric-field antinodes.

Here, we demonstrate electric-dipole coupling of Rydberg states of ultracold atoms, trapped on a superconducting chip, to the microwave field of an on-chip coplanar microwave resonator. The coherent interaction is revealed and characterized by cavity driven Rabi oscillations between the atomic Rydberg states, which are observed by means of state-selective field ionization. The achieved coupling strengths between the atoms and microwave cavity is three orders of magnitude larger than previously observed [23]. We identify and discuss the current main limiting factors for the coupling rates and coherence times and outline strategies for further enhancements and optimization in future devices. Our results are a stepping stone towards the realization of cold-atom - superconductor hybrid quantum systems with unique properties, that can enable switchable, resonator-mediated long-range interactions between the atoms [25], conditional excitation of distant atoms and the realization of quantum gates [25,32–34], coherent microwave to optical photon conversion via single atoms or atomic ensembles [22,30,31], and state transfer from solid-state quantum circuits to optical photons via atoms [35].

II. EXPERIMENTAL APPARATUS

Our hybrid quantum system consists of a cloud of ultracold rubidium atoms trapped on an integrated superconducting

(SC) atom chip containing a coplanar waveguide (CPW) resonator on the chip surface [see Fig. 1(a)]. The experiment is performed in an ultrahigh-vacuum chamber at a pressure of 6×10^{-11} mbar. The SC atom chip is attached to a He-flow cryostat with the surface temperature adjusted to 4.5 K. A chip-based magnetic trap for ultracold atoms is created via the field of the current in a Z-shaped trapping wire, the field associated with persistent SC currents in the resonator, and an external field generated by macroscopic wires and coils [see Fig. 1(b)]. The resulting trapping potential, with an offset field of 3.4 G at the trap center, has a harmonic shape and can trap an atom cloud at a distance of $130\ \mu\text{m}$ from the chip surface. A cloud of cold ^{87}Rb atoms is loaded into the magnetic trap and shifted into the field mode of the standing-wave microwave (MW) resonator, similar to Refs. [17,23,37] (see Appendix A for more details). The atom cloud is positioned close to an electric-field antinode of the third harmonic of the MW resonator at frequency $\omega_c \simeq 2\pi \times 20.55\ \text{GHz}$ [see Fig. 1(c)]. The resonator is inductively coupled via a feedline to an external coherent and tunable MW source. A laser system is used for imaging the atomic cloud and for Rydberg excitation of the atoms. Strong electric-dipole coupling between the atoms and the MW cavity field requires, on the one hand, placing the Rydberg atoms close to the chip surface, and, on the other hand, tuning the frequency of an appropriate

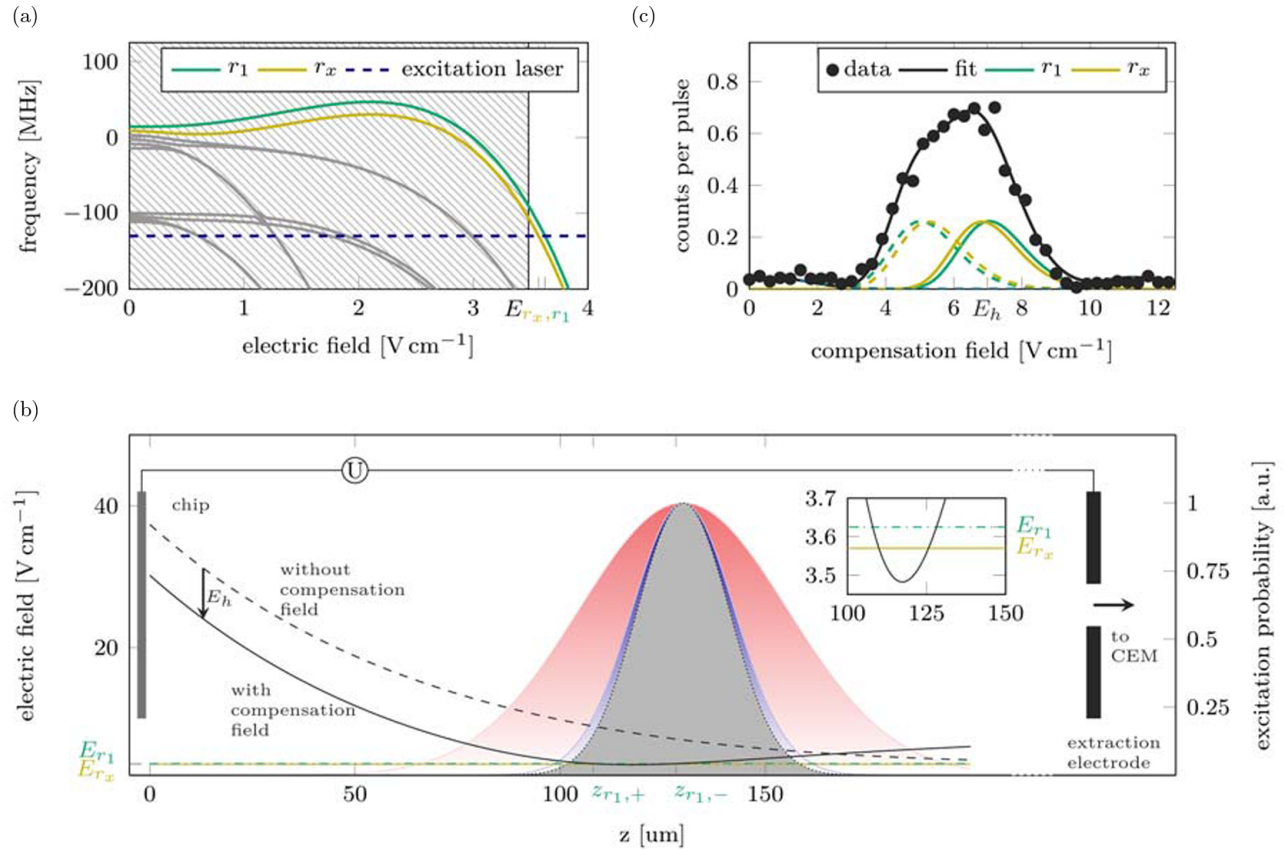


FIG. 2. Laser excitation of Rydberg states of atoms in external fields. (a) Stark map of Rydberg states in the vicinity of the $48D$ state in a magnetic field of 3.4 G. The energies (frequency detuning relative to the $48D$ state in zero electric field) of the Stark states in the varying electric field are indicated by solid lines, while the dashed line indicates the frequency of the excitation laser detuned by $-2\pi \times 130$ MHz. The target state $|r_1\rangle$ (green line) is resonantly excited by the laser in a field of $E_{r_1} = 3.625$ V/cm, and the nearby state $|r_x\rangle$ (yellow line) is resonant at $E_{r_x} = 3.570$ V/cm. Adsorbate field components parallel to the chip surface cannot be compensated, preventing the excitation of Rydberg states in the hatched area. (b) Adsorbates on the chip surface produce an inhomogeneous electric field (black dashed line) that falls off exponentially with the distance from the surface. A voltage U applied between the chip and the extraction electrode creates a homogeneous electric field of $E_h = 7.2$ V/cm that partially compensates the z component of the adsorbate field at the position of the atom cloud (red profile). This leads to a minimum of the total field magnitude (black solid line) at a distance of $z_{\min} = 117$ μm from the chip surface (see the inset for a magnified view of this area). Due to noncompensated field components in the xy plane, the total field magnitude has a parabolic form around the minimum (see Appendix B). State $|r_1\rangle$ is resonantly excited in thin atomic layers at positions $z_{r_1} = 108$ μm and 128 μm where the field is E_{r_1} , while state $|r_x\rangle$ is resonantly excited at positions $z_{r_x} = 110$ μm and 126 μm where the field is E_{r_x} . The excitation probability at each of these positions is proportional to the product (gray profile) of the cloud density (red profile) and the laser intensity (blue profile), and the corresponding atomic transition probabilities to states $|r_1\rangle$ and $|r_x\rangle$. Applying a high-voltage ramp between the chip and the extraction electrode results in field ionization of Rydberg atoms and acceleration of the resulting ions towards the ion detector (CEM). (c) Mean number of Rydberg excitations (ion counts, black dots) per laser pulse versus the applied compensation field. The experimental data are fit by a sum of individual contributions from the $|r_1\rangle$ (green) and $|r_x\rangle$ (yellow) Rydberg states within two excitation layers (solid and dashed lines) each. From the fit we deduce the characteristic parameters of the adsorbate field.

Rydberg transition of the atoms into resonance with the fixed frequency of the cavity mode. A DC electric field applied via the electrode can state-selectively ionize the Rydberg state atoms and extract the resulting ions for detection via a channel electron multiplier (CEM).

A. Rydberg-state excitation

The trapped atoms are excited from the ground state $|5S\rangle$ to a Rydberg state $|r_1\rangle$ in the $48D_{5/2}$ manifold by a two-photon transition, via an intermediate nonresonant state $|5P\rangle$, using a pair of laser pulses with wavelengths 780 and 480 nm. The

atoms are subject to a spatially varying DC (static) electric field, which is the sum of an inhomogeneous field produced by adsorbates on the chip surface [38–41] and a controlled homogeneous compensation field produced by the extraction electrode [see Fig. 1(a)]. The electric field results in strong level shifts of the atomic Rydberg states. Figure 2(a) shows the calculated Stark map of Rydberg states in the vicinity of the zero-field $48D$ state, taking into account the offset magnetic field of the trap. The calculation employs a diagonalization of the atomic Hamiltonian in the presence of electric and magnetic fields [42,43], with the eigenvalues yielding the Rydberg energy spectrum for each field value. Together with state $|r_1\rangle$,

another Rydberg state $|r_x\rangle$ from the $48D_{5/2}$ manifold can also be excited by the laser pulses. The energy levels $|r_1\rangle$ and $|r_x\rangle$ are degenerate in zero magnetic field, but our offset magnetic field lifts the degeneracy, as seen in Fig. 2(a). Level $|r_x\rangle$ is then sufficiently shifted away from the cavity resonance and does not participate in the atom-cavity coupling, as detailed in Sec. II B, while the contribution from $|r_x\rangle$ can be removed from the measured ion signals, as detailed in Sec. II C. The electric field of the adsorbates falls off exponentially from the chip surface. An appropriate voltage applied to the extraction electrode creates a homogeneous field between the chip surface and the electrode, which compensates the z component of the adsorbate field at a desired position z_{\min} within the atomic cloud. Since the adsorbate field is inhomogeneous, the total field strength increases in both directions from z_{\min} along z . Furthermore, the adsorbates produce a nonvanishing field component parallel to the chip surface, in the xy plane, which cannot be compensated for in our setup. This field component thus determines the minimal achievable field strength, while the total electric field in the z direction acquires a parabolic form [see Fig. 2(b) and Appendix B]. Hence, the resonance conditions for Rydberg excitations strongly vary across the atom cloud and each Rydberg state can be laser excited only in a thin ($\lesssim 0.3 \mu\text{m}$) atomic layer. Since the energies of the Stark eigenstates depend only on the absolute value of the electric field, for each Rydberg state there are typically two resonant excitation layers, one on each side of the field minimum at z_{\min} [see the inset of Fig. 2(b)]. By varying the compensation field, these resonant layers can be shifted through the cloud. To match the position of resonant layers with that of the atomic cloud and the excitation laser beams, we vary the compensation field and count the number of Rydberg atoms excited by the laser with fixed detuning $-2\pi \times 130$ MHz with respect to the zero-field $48D_{5/2}$ state. To this end, we prepare a cold atomic cloud in the mode volume of the CPW cavity, at a distance of $130 \mu\text{m}$ from the chip surface. The cloud is exposed to a series of 300 excitation pulses of $1 \mu\text{s}$ duration, followed by Rydberg atom detection, at 3 kHz repetition rate, without significantly reducing the number of trapped atoms. After each pulse, the Rydberg excited atoms are ionized by a $1 \mu\text{s}$ electric-field ramp and the resulting ions are subsequently detected by the CEM with a detection efficiency $>50\%$ [44,45]. Figure 2(c) shows the mean number of ion counts per excitation pulse as a function of the compensation field. We excite on average on the order of one Rydberg atom per pulse, which allows us to disregard interactions between the Rydberg atoms. The resulting dependence of the ion count on the compensation field maps the atomic density distribution and the laser intensity profile in different excitation layers. The latter is deduced from fitting an appropriate model function to the experimental data (see Appendix B). We then obtain that the exponential decay length of the adsorbate field from the chip surface is $\zeta \simeq 70 \mu\text{m}$, while the field component parallel to the chip surface has a value of $3.482(14)$ V/cm. For a compensation field of 7.2 V/cm, only two Rydberg states $|r_1\rangle$ and $|r_x\rangle$ are excited with significant probabilities in the center of the atom cloud. The calculated two-photon transition amplitudes between the ground $|5S\rangle$ and the Rydberg states $|r_1\rangle$ and $|r_x\rangle$ are approximately equal, which corresponds to similar excitation numbers N_{r_1} and N_{r_x} .

B. Tuning the Rydberg transition

With an atom in Rydberg state $|r_1\rangle$, depending on the total electric and magnetic fields at the atomic position, there are many possible MW transitions to the Rydberg states in the $n = 47$ manifold. In Fig. 3(a) we show the calculated Stark map for the Rydberg states of atoms in the 3.4 G offset magnetic field of the trap and varying total electric field. Given the resonant frequency of the cavity field ω_c and the total electric field $E_{r_1} = 3.625$ V/cm at the position of the layer of atoms in state $|r_1\rangle$, we find a suitable resonant transition to a Rydberg state $|r_2\rangle$ in the $n = 47$ manifold [see Fig. 3(b)]. Our calculations also yield the dipole moments for different transitions (see Appendix C) and we obtain the dipole moment $d \simeq 30ea_0$ for the $|r_1\rangle \rightarrow |r_2\rangle$ transition. The differential Stark shift between levels $|r_1\rangle$ and $|r_2\rangle$ is rather small, -163 MHz/(V/cm). Moreover, neighboring Rydberg states are sufficiently far off-resonant, which suppresses their excitation.

C. Rydberg ionization signal

Using the electric-field ramp of the extraction electrode, we ionize the Rydberg state atoms and detect the resulting ions. In principle, each state ionizes under the influence of an electric-field ramp with a characteristic time dependence, which can be used to distinguish the Rydberg states [46,47]. Generally, states with higher principal quantum numbers n tend to ionize earlier, while states with higher orbital angular momenta L and magnetic quantum numbers m_j are ionized later [48]. In practice, the ionization signal from neighboring Rydberg states can have large temporal overlap, complicating their unambiguous discrimination. In Fig. 3(c), upper panel, we show three examples of calculated ionization signals from different Rydberg states subject to the same electric-field ramp (see Appendix D). If we divide the ion arrival times into two intervals T_1 and T_2 , then, during T_1 , we detect all the ions from state $48D$ and some of the ions from states $n = 47$, while the ions detected during T_2 only originate from states with $n = 47$. This is the main reason for choosing the resonant state $|r_2\rangle$ in the $n = 47$ manifold, despite a relatively small dipole moment of the MW transition between states $|r_1\rangle$ and $|r_2\rangle$, as compared with other transitions with larger dipole moments. In the experiment, we populate the Rydberg states $|r_x\rangle$ and $|r_1\rangle$ with comparable probabilities via laser excitation, $N_{r_x}/N_{r_1} = a \approx 1$, and then couple $|r_1\rangle$ to state $|r_2\rangle$ via the resonant MW cavity field. The electric-field ramp results in the Rydberg state ionization and detection of $N = N_{r_x} + N_{r_1} + N_{r_2}$ ions. All the ions N_{r_x} and N_{r_1} from states $|r_x\rangle$ and $|r_1\rangle$ are detected during the time interval $T_1 = 1.8\text{--}2.0 \mu\text{s}$, while we estimate that the N_{r_2} ions from state $|r_2\rangle$ are detected during the time interval $T_2 = 2.0\text{--}2.1 \mu\text{s}$ with probability $p = 0.34$ and during T_1 with probability $(1 - p) = 0.66$. Hence, the number of ions N_{T_1} and N_{T_2} detected during T_1 and T_2 are $N_{T_1} = N_{r_x} + N_{r_1} + (1 - p)N_{r_2} \simeq (1 + a)(N_{r_1} + N_{r_2}) - pN_{r_2}$ and $N_{T_2} = pN_{r_2}$, while $N_{T_1} + N_{T_2} = N$ and $N_{r_x} = a(N_{r_1} + N_{r_2})$ after the MW transfer. We then obtain that the population of state $|r_2\rangle$ is

$$\rho_{22} \equiv \frac{N_{r_2}}{N_{r_1} + N_{r_2}} = \frac{N_{T_2}}{p} \frac{(1 + a)}{N_{T_1} + N_{T_2}} = \frac{1 + a}{p} p_2,$$

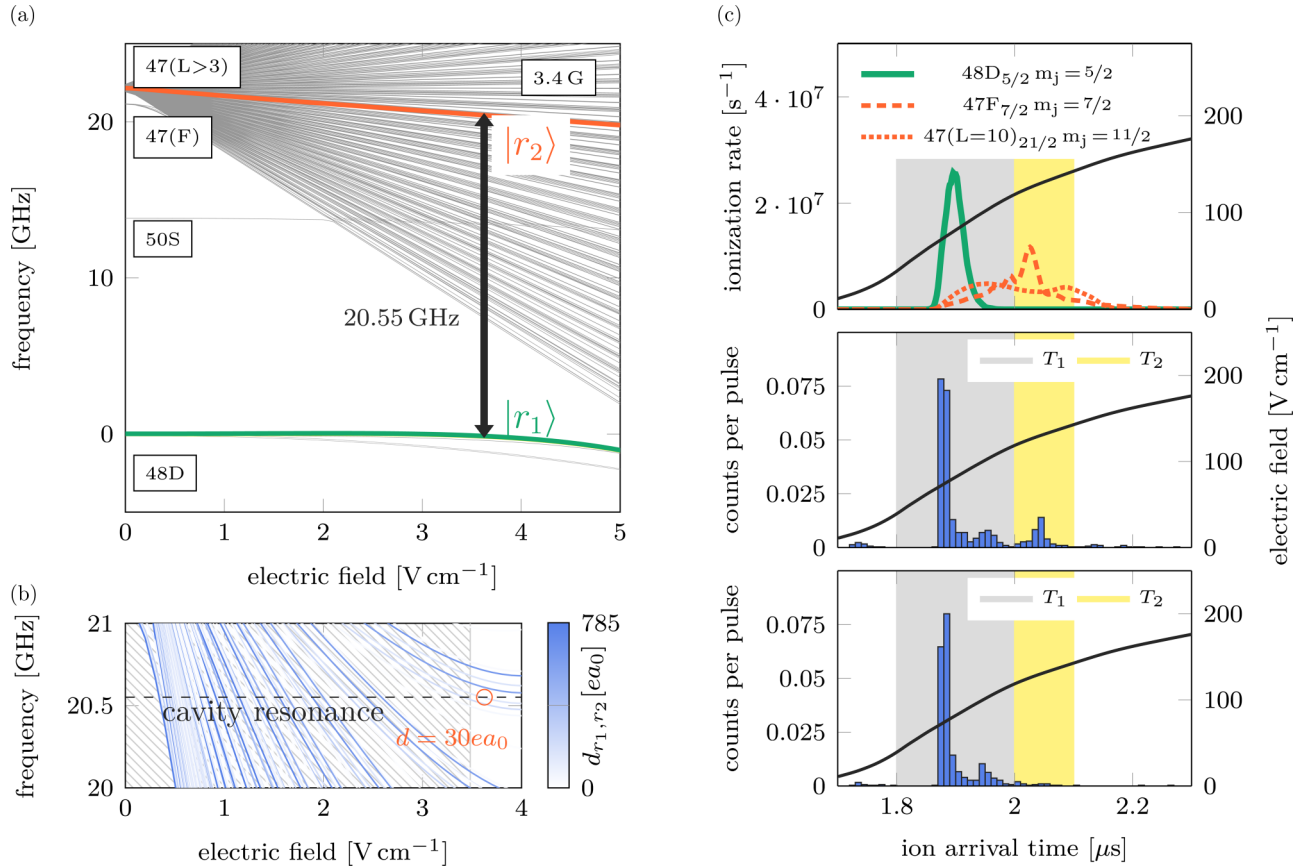


FIG. 3. Rydberg transition and state detection. (a) Stark map of Rydberg states in the vicinity of 48D and 47($L \geq 3$) states in a magnetic field of 3.4 G. State $|r_1\rangle$ (green line) is resonantly excited by a laser in an electric field of $E_{r_1} = 3.625$ V/cm [see Fig. 2(a)] and is coupled by a MW photon with frequency $\omega_c = 2\pi \times 20.55$ GHz to the Rydberg state $|r_2\rangle$ (red line) in the 47($L > 3$) manifold. (b) Relative frequencies (solid lines) and dipole moments (opacity) for transitions from state $|r_1\rangle$ to the states in the $n = 47$ manifold, assuming in the calculations the total electric field along x , the magnetic field along y , and linear MW field polarization in the z direction. The dashed horizontal line indicates the cavity resonance frequency ω_c and the transition to the resonant state $|r_2\rangle$ (red circle) has a dipole moment of $d = 30ea_0$. Transitions with dipole moments smaller than $d = 10^{-3}ea_0$ are not shown. (c) Upper panel shows examples of calculated ionization rates for three Rydberg states (green, red dashed, and red dotted lines) upon the electric field ramp (black line) (see Appendix D). Central panel shows a histogram of the ion arrival times (blue bars) as measured for a laser Rydberg excitation followed by a MW π pulse of 250 ns duration and a subsequent electric field ramp (black solid line). The data are averaged over 25 experimental cycles with 300 excitation-interaction-detection sequences in each cycle. Defining two time intervals T_1 and T_2 permits us to distinguish the ion signal from states $|r_1\rangle$ and $|r_2\rangle$. Lower panel shows the ion arrival time distribution without MW pulses.

where $p_2 \equiv N_{T_2}/N$. In Fig. 3(c), middle panel, we show the measured ion signal after applying a MW π pulse, which would ideally transfer all of the population of state $|r_1\rangle$ to state $|r_2\rangle$. The ion arrival times have a large peak in T_1 originating from all states $|r_x\rangle$, $|r_1\rangle$, $|r_2\rangle$, and a smaller peak in T_2 that we attribute only to state $|r_2\rangle$. With $N_{T_1}/N_{T_2} \approx 5.6$, the population of state $|r_2\rangle$ is $\rho_{22} \approx 0.9$, consistent with a weakly damped half of a resonant Rabi cycle. Without the MW pulse, all the population remains in states $|r_x\rangle$ and $|r_1\rangle$ and no peak is observed in T_2 , as shown in the lower panel of Fig. 3(c).

III. CAVITY-DRIVEN RYDBERG TRANSITION

Having described all the necessary ingredients of our system, we now turn to the demonstration of coherent coupling of the atomic Rydberg transition to an externally pumped MW field mode of the cavity. The experimental sequence is illustrated in Fig. 4(a): after the two-photon laser excitation of

the atoms to the Rydberg state $|r_1\rangle$, we inject into the cavity a MW pulse of variable power and duration. The Rydberg atom interacts with the cavity field on the transition $|r_1\rangle - |r_2\rangle$ for up to 1.5 μ s. The cavity-induced population transfer between the Rydberg states is then detected via selective field ionization and time-resolved ion counting. The interaction of the atom with the MW cavity field can be well approximated by a two-level model. The field mode of the cavity with frequency $\omega_c = 2\pi \times 20.55$ GHz is resonant with the atomic transition $|r_1\rangle - |r_2\rangle$, while the next-nearest Rydberg transition is detuned by at least 35 MHz [see Fig. 3(b)], which exceeds the cavity linewidth $\kappa = 2\pi \times 9$ MHz and the maximal achieved Rabi frequency $\Omega_{\max} \approx 2\pi \times 8$ MHz. There are no near resonant transitions from state $|r_x\rangle$. Decay to other states is negligible during the entire excitation, interaction, and measurement time of ≈ 3 μ s, which is much shorter than the Rydberg state lifetime $1/\Gamma \approx 60$ μ s [49,50]. In Fig. 4(b) we show the Rydberg transition spectrum of the

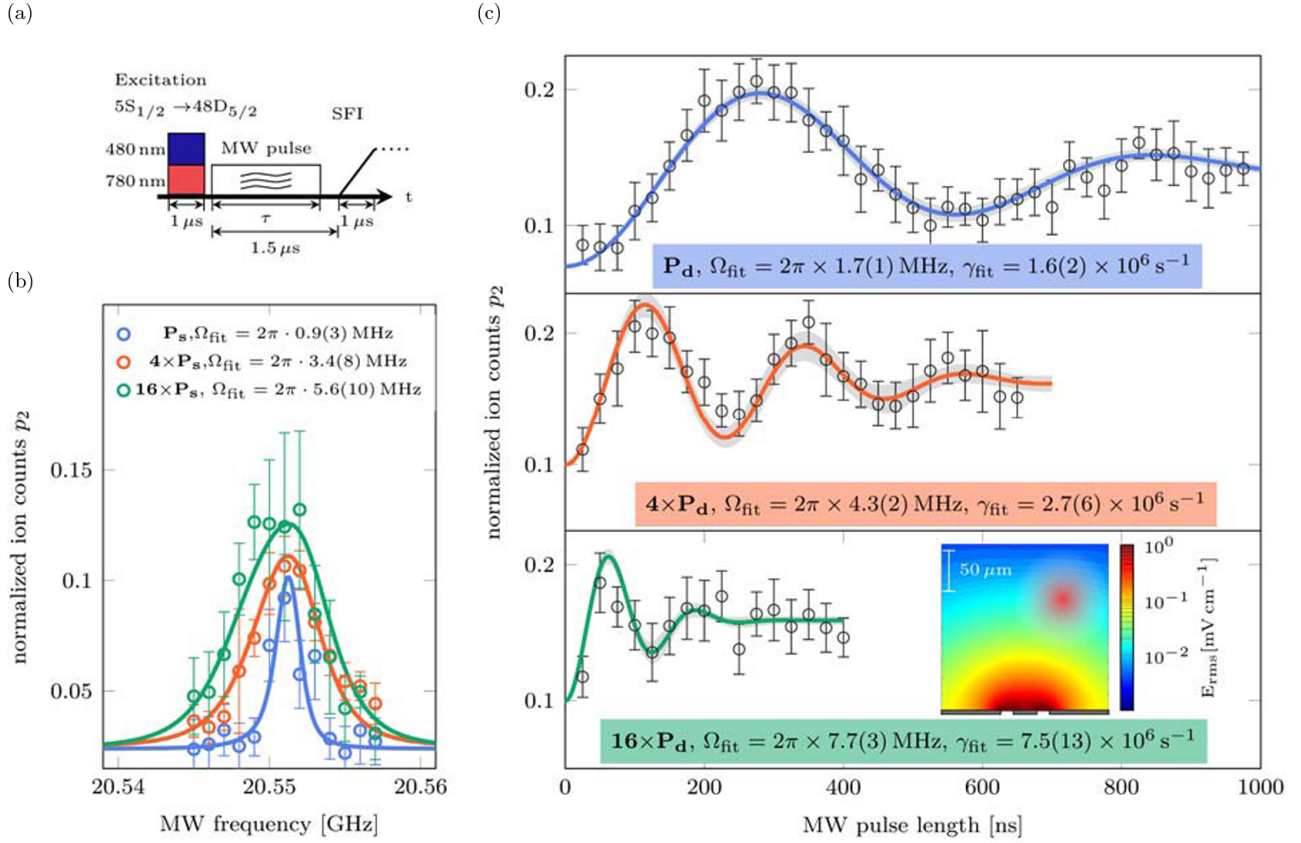


FIG. 4. Coupling Rydberg transition to pumped MW cavity mode. (a) Schematics of the experimental sequence involving optical excitation of the atoms to the Rydberg state by a two-photon laser pulse of $1 \mu\text{s}$ duration, injection into the cavity a MW pulse of variable power and duration $\tau \leq 1.5 \mu\text{s}$, interaction of the Rydberg excited atoms with the MW cavity field, and selective field ionization (SFI) and detection of the Rydberg atoms by a $1 \mu\text{s}$ electric-field ramp from 7.2 V/cm to about 210 V/cm . In each experimental cycle, the atom cloud is exposed to a series of 300 excitation-interaction-detection sequences at a repetition rate of 3 kHz. MW leakage through the electronic switches and background counts lead to a small offset of the ion signal. (b) Normalized ion count $p_2 = N_{r_2}/N$ (open circles), proportional to the population ρ_{22} of Rydberg state $|r_2\rangle$, versus the frequency of the MW pulses ($\tau = 1.5 \mu\text{s}$) injected into the cavity, for three different powers P_s , $4P_s$, $16P_s$ (blue, red, green) of the MW source. Each data point is obtained by averaging over ten experimental cycles, with error bars denoting ± 2 standard deviations. We fit the data by theoretical excitation spectra (solid lines of the same color) to deduce the Rabi frequencies $\bar{\Omega}$ of the MW field resonant with the $|r_1\rangle \rightarrow |r_2\rangle$ transition. (c) Dynamics of population of Rydberg state $|r_2\rangle$ (proportional to ion count p_2) for three different powers P_d , $4P_d$, $16P_d$ of the injected MW field at frequency $\omega_{\text{MW}} = 20.551 \text{ GHz}$. Each data point (open circle) is obtained by averaging over 25 experimental cycles, with error bars denoting ± 2 standard deviations. Rabi frequencies Ω_{fit} and decoherence rates γ_{fit} are obtained by fitting the model function (see the text and Appendix E for details), with the fitted curves (solid lines) shown with 95% confidence bounds (gray). The inset shows the MW cavity field strength in the xz plane for a rms ground-state voltage of $3 \mu\text{V}$ (see Appendix C), with the cloud placed at a distance of $z \simeq 130 \mu\text{m}$ from the chip surface (bottom) and laterally displaced from the central cavity conductor by $x \simeq 50 \mu\text{m}$. The gray bars indicate the position of the CPW. We note that P_d and P_s are not necessarily the same (see Appendix A on the microwave cavity).

atoms interacting with the intracavity MW field pumped by the external source of variable frequency at three different powers. The exposure time of $1.5 \mu\text{s}$ is sufficiently long for the atomic populations to attain the steady state. We fit the observed spectrum with a model function corresponding to the steady-state population ρ_{22} of the Rydberg state $|r_2\rangle$, while the Rabi frequency of the MW field also depends on the frequency injected into the cavity field (see Appendix E). We assume that the main contribution to the atomic spectral linewidth comes from the inhomogeneous broadening $\Delta\omega_{12} \simeq 2\pi \times 1.1 \text{ MHz}$ of the transition $|r_1\rangle - |r_2\rangle$ due to the differential Stark shift of -163 MHz/(V/cm) between levels $|r_1\rangle$ and $|r_2\rangle$ in the inhomogeneous electric field varying by 0.0067 V/cm within the resonantly excited atomic layer of widths $\lesssim 0.3 \mu\text{m}$ (see Appendix C). In comparison, the natural linewidth (decay

rate) $\Gamma \simeq 2\pi \times 2.7 \text{ kHz}$ of the Rydberg state is negligible. For stronger pumping fields, the spectrum is dominated by power broadening. For each pumping power, we extract the peak Rabi frequency $\bar{\Omega}$ at the pump MW frequency $\omega_{\text{MW}} \simeq \bar{\omega}_{12}$ resonant with the mean transition frequency of the atoms in the resonant layer $\bar{\omega}_{12}$. We then obtain that the peak Rabi frequency $\bar{\Omega}$ scales approximately as the square root of the pumping power P , as expected for a resonant one-photon transition. By changing the detuning of the excitation lasers, we can excite the Rydberg states of atoms in a different resonant layer. This in turn will shift the atomic Rydberg transition out of the cavity resonance, causing the signal in Fig. 4(b) to disappear. Using a MW antenna from outside the chamber, we can recover the ionization signal for an appropriate MW frequency, which verifies that the Rydberg MW transition is

indeed driven by the cavity field. The cavity and the atomic resonance are, however, not perfectly aligned, which leads to a small asymmetry of the resonance profiles that becomes more pronounced for increasing MW power, as seen in Fig. 4(b). We then fix the frequency of the injected MW field to $\omega_{\text{MW}} = 2\pi \times 20.551$ GHz, and investigate the dynamics of the Rydberg transition by varying the duration of the MW pulse for three different input powers. In Fig. 4(c) we show the normalized ion count p_2 from the upper Rydberg state $|r_2\rangle$ as a function of the MW pulse duration. We observe damped Rabi oscillations between states $|r_1\rangle$ and $|r_2\rangle$ with the Rabi frequencies that scale approximately as $\Omega \propto \sqrt{P}$, similarly to the steady-state case above. We approximate the population difference between the Rydberg states as $\bar{D} = \rho_{11} - \rho_{22} = \exp(-t^2/\tau_{\text{damp}}^2) \cos(\Omega t)$, which follows from a simple model (see Appendix E) that assumes two-level atoms coherently driven by spatially varying Rabi frequencies corresponding to an inhomogeneous MW cavity field distribution across the laterally displaced atomic ensemble, as shown in the inset of Fig. 4(c). The corresponding damping rate $\gamma = 1/\tau_{\text{damp}}$ then scales approximately linearly with the Rabi frequency, $\gamma \simeq \frac{b}{\sqrt{2}}\Omega$ with the proportionality constant $b \approx 0.2$ that quantifies the relative change of cavity MW field across the atomic cloud along the x direction.

IV. CONCLUSIONS

In this work, we have demonstrated coherent electric-dipole coupling between a superconducting coplanar MW resonator and ultracold Rydberg atoms trapped on an integrated atom chip. We used DC electric fields to fine-tune the atomic Rydberg transition and observed resonant Rabi oscillations between a pair of Rydberg states driven by the externally pumped MW field of the cavity. Using the Rydberg transition of the atoms, we achieved three orders of magnitude increase in the atom-cavity coupling strength, as compared with the magnetic-dipole coupling on the ground-state hyperfine transition used in our previous experiment [23]. The observed damping of the Rabi oscillations is dominated by the spread of Rabi frequencies for the Rydberg atoms in different positions of the layer resonantly excited by the laser. In comparison, the real single atom decoherence is much smaller, and individual Rydberg atoms are expected to exhibit much longer coherence times. We note that the damping rate of the Rabi oscillations originating from the variations of the cavity field at different positions within the atom cloud is significantly reduced by the resonant laser excitation of Rydberg states of atoms in a thin layer at a well defined distance from the atom chip. If we had used spatially homogeneous, narrow-linewidth excitation of atoms close to the chip surface [16], the large variation of the cavity MW field across the atomic cloud would have precluded observation of coherent Rabi oscillations. Reducing the lateral size of the excitation layer by employing vector field and field gradient control and using narrow-line excitation lasers can further decrease or completely eliminate the cavity-field variations for the Rydberg excited atoms, which in turn enhance the coherence. The atoms in our system are trapped relatively far from the CPW cavity, $130 \mu\text{m}$ from the chip surface, and the resulting vacuum Rabi frequency $\Omega_{\text{vac}} = dE_c^{(0)}/\hbar = 2\pi \times 0.6$ kHz is smaller than the cavity linewidth

$\kappa \simeq 2\pi \times 9$ MHz. Several improvements can be made: The atoms can be brought closer to the chip surface and, e.g., at a distance of $\approx 10 \mu\text{m}$ the cavity field strength $E_c^{(0)}$ will increase by more than an order of magnitude. At smaller distances, the stronger adsorbate fields should be treated more carefully and a pair of Rydberg-Stark eigenstates with much larger dipole moments $d \simeq 10^3 ea_0$ and a small differential Stark shift can be identified and employed [51]. Finally, next-generation integrated devices can have better optimized architectures. A significant increase of the electric microwave field amplitude could be achieved by using a quarter-wave resonator with a fundamental mode frequency of 20.55 GHz or by designing an appropriate lumped element LC circuit. This approach also has the potential to produce a more homogeneous microwave field which would reduce dephasing of the Rabi oscillations. Furthermore, there has been great progress in increasing the quality factors of superconducting coplanar waveguide resonators, already exceeding 10^6 at ≈ 50 mK temperatures [52], which also enables coherent operations of SC qubits. This will bring the strong-coupling regime of single Rydberg atoms and SC qubits to single MW cavity photons within experimental reach.

ACKNOWLEDGMENTS

This work was supported by the Deutsche Forschungsgemeinschaft through SPP 1929 (GiRyd), Project No. 394243350 (CIT) and Project KL 930/16-1. C.G. acknowledges financial support from the Evangelische Studienwerk Villigst e.V.

APPENDIX A: EXPERIMENTAL SYSTEM

1. Atomic cloud

Starting with ^{87}Rb atoms in a conventional magneto-optical trap, about 5×10^7 atoms in the ground state $|5S_{1/2}, F=2, m_F=2\rangle$ are loaded into a magnetic quadrupole trap. The atoms are then moved to a Ioffe trap for evaporative cooling. Using optical tweezers, the ultracold atomic cloud is transferred to a superconducting atom chip, which is mounted on the cold finger of a He-flow cryostat. At the chip, the spin-polarized atomic cloud is loaded into a magnetic microtrap generated by a current in the Z-shaped trapping wire and other external homogeneous fields. Additional bias fields are used to finally position the cloud close to a coplanar waveguide resonator. Using standard absorption imaging, we verify that the cloud is trapped at $130 \mu\text{m}$ distance to the chip surface. The trapping potential has a parabolic shape with trap frequencies $\omega_{x,y,z} = 2\pi \times 61$ Hz. The offset field at the trap center is about 3.4 G. The atom cloud has almost spherical shape with a cloud diameter (full width at half maximum) of $60 \mu\text{m}$. The atom number in the cloud is 7×10^4 , the peak density is $2.7 \times 10^{11} \text{ cm}^{-3}$ and the temperature is $1 \mu\text{K}$. More details on the loading and trapping procedure are given in Ref. [23].

2. Rydberg lasers

The atoms are excited from the ground state $|5S_{1/2}\rangle$ to the Rydberg states by a pair of laser pulses with wavelengths 780

and 480 nm and duration of 1 μ s, while the intermediate state $|5P_{3/2}\rangle$ is detuned by 160 MHz. Both laser beams are centered at the atomic cloud. With beam waists ($1/e^2$ radii) of 5.45 and 0.025 mm and laser powers of 0.5 and 25 mW, the peak intensities of the red and blue lasers are 0.001 and 2500 W/cm², respectively. The red laser is phase locked to a commercial frequency comb with an absolute frequency accuracy of 2 kHz and linewidth below 10 kHz. The blue laser is stabilized with a wavelength meter (HighFinesse WSU) to an absolute frequency accuracy better than 2 MHz and a linewidth better than 200 kHz. In zero-field conditions, the single-photon Rabi frequencies for individual transitions $5S_{1/2}$ - $5P_{3/2}$ and $5P_{3/2}$ - $48D_{5/2}$, averaged over all magnetic substates and possible transitions, are $2\pi \times 3.6$ MHz and $2\pi \times 36$ MHz, respectively. The resulting two-photon Rabi frequency for the Rydberg excitation $5S_{1/2}$ - $48D_{5/2}$ is $2\pi \times 400$ kHz. Taking into account the external fields and applying the selection rules for appropriate laser polarization, the two-photon Rabi frequency for the transition $|5S_{1/2}, F=2, m_F=2\rangle \rightarrow |r_1\rangle$ and $|r_x\rangle$ is reduced to about $\Omega_{gr} = 2\pi \times 30$ kHz; the ratio a between these Rabi frequencies depends on the unknown direction of the lateral surface field (see Appendix B) and is assumed $a \approx 1$. With this Rabi frequency and a pulse duration of 1 μ s applied to the ensemble of 7×10^4 ground-state atoms, we excite on average about one atom to the Rydberg state $|r_1\rangle$.

3. Microwave cavity

The on-chip superconducting coplanar waveguide cavity is a $\lambda/2$ transmission line resonator with the fundamental mode frequency $\omega_0 = 2\pi \times 6.85$ GHz. To drive the transition between the Rydberg states $|r_1\rangle$ and $|r_2\rangle$, we use the third harmonic of the resonator having the frequency $\omega_c = 2\pi \times 20.55$ GHz, the linewidth $\kappa = 2\pi \times 9$ MHz and the corresponding quality factor $Q \approx 2300$. Within the temperature range where the resonator is superconducting, the resonance frequency can be tuned by about 30 MHz. For driving purposes, the resonator is inductively coupled to a MW feedline and connected to a commercial MW signal generator (Rohde & Schwarz SMF100A) with a linewidth < 1 Hz. The MW electric field in the resonator is then

$$E_c = D_c \frac{\sqrt{P}}{\kappa/2 - i(\omega_{MW} - \omega_c)}, \quad (\text{A1})$$

where P is the power of the MW field at frequency ω_{MW} injected into the resonator. The proportionality factor D_c is then mainly given by damping due to the microwave cables and connections. It may be different for individual cool downs of the cryostat, due to varying mechanical stress on the MW cable connections during this procedure.

APPENDIX B: RYDBERG EXCITATION

1. Surface fields

The adsorbates on the chip surface produce an inhomogeneous electric field. We approximate the z component of this adsorbate field perpendicular to the chip surface as $E_{ad,z}(z) = E_0 e^{-z/\zeta}$, where ζ is a decay length. This component is partially compensated by a homogeneous field E_h between the

extraction electrode and the grounded atom chip surface. The compensation field can be freely adjusted by the voltage U applied to the extraction electrode. The inhomogeneous adsorbate distribution leads to an additional field component parallel to the chip surface, $E_{ad,xy}$, which cannot be compensated for in our system. The total electric field

$$E(z) = \sqrt{(E_0 e^{-z/\zeta} - E_h)^2 + E_{ad,xy}^2} \quad (\text{B1})$$

can then be tuned via the compensation field E_h and has a parabolic form around the field minimum $E(z_{\min}) = E_{ad,xy}$ at $z_{\min} = \zeta \ln \frac{E_0}{E_h}$.

2. Excitation layers

The Stark shifts of the atomic Rydberg levels in a DC electric field depend only on the absolute field strength. Within the atomic cloud, there can be two layers where the electric field has a specific value $E_r > E(z_{\min}) = E_{ad,xy}$. These layers are positioned on both sides of the field minimum at

$$z_{r,\pm} = z_{\min} - \zeta \ln \left(1 \pm \sqrt{\frac{E_r^2 - E_{ad,xy}^2}{E_h^2}} \right). \quad (\text{B2})$$

A Rydberg state $|r\rangle$ that is resonant at a specific field strength E_r is thus excited in two excitation layers at position $z_{r,\pm}$. For a field $E_r = E_{ad,xy}$ both layers merge at $z_{r,\pm} = z_{\min}$, while no excitation can take place for states that are resonant in fields $E_r < E_{ad,xy}$. The local field gradient in a resonant excitation layer is

$$\alpha_{r,\pm} = \left. \frac{dE}{dz} \right|_{z_{r,\pm}} = \frac{1}{\zeta} \frac{E_r^2}{E_r} (\beta \mp \sqrt{\beta_r}), \quad (\text{B3})$$

with $\beta_r = (E_r^2 - E_{ad,xy}^2)^{1/2}/E_h$. Assuming that the two-photon Rabi frequency Ω_{gr} is small compared with the linewidth of the excitation laser $\Delta\omega_{las}$, the width of the excitation layer can be estimated as

$$\Delta z_{r,\pm} = \frac{\Delta\omega_{las}}{d_r \alpha_{r,\pm}}, \quad (\text{B4})$$

where d_r is the Stark gradient, or static dipole moment, of state $|r\rangle$.

3. Excitation probability

With the excitation layers oriented parallel to the chip surface, the Rydberg excitation probability of the atoms within a single layer at z is proportional to the atomic line density and the laser intensity profile,

$$n(z) \propto \exp\left(-\frac{(z - z_{\text{cloud}})^2}{2\sigma^2}\right), \quad (\text{B5})$$

$$I(z) \propto \exp\left(-\frac{2(z - z_{\text{beam}})^2}{w^2}\right), \quad (\text{B6})$$

where z_{cloud} is the position of the atomic cloud, σ is the cloud radius, z_{beam} is the laser beam center, and w is the beam waist. For a two-photon transition, $\Omega_{gr} \propto \sqrt{I_{780} I_{480}}$, the effective beam waist is $w = w_{780} w_{480} / (w_{780}^2 + w_{480}^2)^{1/2}$ with the individual beam waists w_{780} and w_{480} assumed to overlap at the same position. The total Rydberg excitation probability

is given by the sum over all possible transitions in the corresponding excitation layers:

$$P_{\text{Ry}} = \sum_r \sum_{s=\pm} A_{r,s} n(z_{r,s}) I(z_{r,s}), \quad (\text{B7})$$

where the strength coefficients $A_{r,\pm}$ depend on the dipole matrix element of the corresponding transition.

4. Fit to the data

We use Eq. (B7) to fit the experimental data in Fig. 2(c), taking into account all states and their corresponding excitation layers. For each state $|r\rangle$, we determine the resonance field value E_r from the Rydberg Stark map calculations in Fig. 2(a) with the excitation laser detuning set to -130 MHz with respect to the zero-field $48D_{5/2}$ state. Atomic cloud and beam parameters are $z_{\text{cloud}} = z_{\text{beam}} = 130 \mu\text{m}$, $\sigma = 25 \mu\text{m}$, and $w \approx w_{480} = 25 \mu\text{m}$, leaving only the strength coefficients A_r and the adsorbate field parameters E_0 , ζ , and $E_{\text{ad},xy}$ as free fitting parameters. We then obtain $E_0 = 37.2(54)$ V/cm, $\zeta = 70 \mu\text{m}$, and $E_{\text{ad},xy} = 3.482(14)$ V/cm. Our measurements indicate that the adsorbate field attains saturation once the experiment is running for some weeks, with a day-to-day variation of the field being less than 1 mV/cm [39]. Rydberg excitations mostly occur in the resonant excitation layers of the two states $|r_1\rangle$ and $|r_x\rangle$ because other states can be resonantly excited in different electric fields, at positions outside of the atomic cloud. For a compensation field of $E_h = 7.2$ V/cm, the two excitation layers for state $|r_1\rangle$ (resonant with the excitation laser at total field $E_{r_1} = 3.625$ V/cm) are located at $z_{r_1,+} = 108 \mu\text{m}$ and $z_{r_1,-} = 128 \mu\text{m}$. With the two-photon excitation linewidth $\Delta\omega_{\text{las}} = 2\pi \times 2$ MHz, the Stark gradient $d_{r_1} = -300$ MHz/(V/cm) and the field gradients $\alpha_{r_1,\pm}$, the corresponding layer widths are $\Delta z_{r_1,+} = 0.21 \mu\text{m}$ and $\Delta z_{r_1,-} = 0.28 \mu\text{m}$. Since the atomic cloud is centered at $z = 130 \mu\text{m}$, dominant excitation takes place in the $z_{r_1,-}$ layer. Energetically close states are excited in layers at different distances from the chip. They contribute to the ion signal, but do not participate in the MW transition between the Rydberg states and therefore only affect the contrast in the Rabi oscillation measurements.

APPENDIX C: MICROWAVE RYDBERG TRANSITION

1. Matrix elements

The energy spectrum of Rydberg states in external fields can be calculated by diagonalization of the atomic Hamiltonian, including the interactions with the magnetic and electric fields, in the basis of zero-field states $|n, l, j, m_j\rangle$ [42]. We compute the energy eigenvalues and the corresponding eigenvectors

$$|r\rangle = \sum_{n,l,j,m_j} \beta^{n,l,j,m_j} |n, l, j, m_j\rangle, \quad (\text{C1})$$

where β^{n,l,j,m_j} are the normalized amplitudes of the basis states. The dipole moment for the transition between a pair of Rydberg states $|r_i\rangle$ and $|r_f\rangle$ is then [43]

$$\vec{d} = e \langle r_f | \vec{r} | r_i \rangle = e \sum_q \sum_{q'} \beta_f^{q'} \beta_i^q \langle q' | \vec{r} | q \rangle, \quad (\text{C2})$$

where e is the electron charge and \vec{r} is its position vector, while q and q' denote the full set of quantum numbers n, l, j, m_j . Note that, for an atom subject to only a magnetic or electric field, only a subset of basis states, determined by the selection rules, may be required for the diagonalization. However, in combined electric and magnetic fields, all the zero-field basis states with different quantum numbers l and m_j should be included, and already for small fields a set of more than 15 000 basis states are required for the results of diagonalization to converge. The precise polarization of the MW field with respect to the directions of the electric and magnetic fields at the excitation position is difficult to measure or simulate. Our calculations of the Rydberg state energies and transition dipoles as per Eqs. (C1) and (C2), assuming the magnetic field of 3.4 G along the y direction, the electric field of 3.625 V/cm in the x direction, and a MW field polarization in the z direction, reproduce the observed transition frequencies well, and we obtain the dipole moment $d \simeq 30ea_0$ for the Rydberg transition $|r_1\rangle \rightarrow |r_2\rangle$. The corresponding dipole moment for the transition $|r_x\rangle \rightarrow |r_2\rangle$ is more than four orders of magnitude smaller. Changing the field strengths and directions can change the resulting transition dipole moments.

2. Vacuum Rabi frequency

The electric-field energy in the cavity per MW photon is $CU_c^2 = \hbar\omega_c$. With the cavity length $l = 9.3$ mm and the capacitance per unit length $C/l = 164$ pF/m, the (rms) ground-state voltage on the central conductor is $U_c = 3 \mu\text{V}$. The resulting electric field per cavity photon at the position of the atoms $z = 130 \mu\text{m}$ below the chip surface and 0.85 mm away from the antinode is $E_c^{(0)}(z) = 0.015$ mV/cm and varies by about 30% over the extent of the cloud. With the MW polarization along the transition dipole moment, the vacuum Rabi frequency is then $\Omega_{\text{vac}} = dE_c^{(0)}/\hbar = 2\pi \times 0.6$ kHz.

3. Rydberg transition linewidth

The Stark gradients (static dipole moments) of the Rydberg states $|r_1\rangle$ and $|r_2\rangle$ are $d_{r_1} = -300$ MHz/(V/cm) and $d_{r_2} = -463$ MHz/(V/cm), leading to a differential Stark shift coefficient $\Delta d_r = d_{r_2} - d_{r_1} = -163$ MHz/(V/cm). As described above, a laser with linewidth $\Delta\omega_{\text{las}} = 2\pi \times 2$ MHz excites the atoms to the Rydberg state $|r_1\rangle$ in a layer of width $\Delta z_{r_1,-} = 0.28 \mu\text{m}$, where the electric field varies by $\Delta z_{r_1,-} \alpha_{r_1,-} = \Delta\omega_{\text{las}}/d_{r_1}$, as per Eqs. (B3) and (B4). Hence, the Rydberg transition $|r_1\rangle \rightarrow |r_2\rangle$ for the atoms in this layer is inhomogeneously broadened by the spatially varying electric field by

$$\Delta\omega_{12} \simeq \Delta z_{r_1,-} \alpha_{r_1,-} \Delta d_r = \Delta\omega_{\text{las}} \frac{\Delta d_r}{d_{r_1}} \simeq 2\pi \times 1.1 \text{ MHz}. \quad (\text{C3})$$

APPENDIX D: IONIZATION SIGNAL

The selective field ionization (SFI) signal for a specific Rydberg state and electric-field ramp is calculated by following the time evolution of the atomic population through the Stark map, using the diagonalization of the Hamiltonian matrix with 2 ns step size. At each time step and for each state,

an ionization rate is calculated in a separate diagonalization of a Hamiltonian additionally containing a complex absorbing potential, $CAP = -i\eta W(\hat{r}, F_E)$, with the scaling parameter $\eta = 1.52 \times 10^{-10} E_H/a_0$ (with Hartree energy E_H and Bohr radius a_0), a r^6 radius dependence and a shift with the external electric field F_E [53]. The time dependence of the electric field corresponds to the voltage ramp at the extraction electrode, while the SFI signal has a time delay of $1.53 \mu\text{s}$ equal to the time of flight of the ions in the experiment. To limit the number of basis states and speed up calculations, the magnetic field is neglected during the ionization process, avoiding thereby mixing the different m_j states in the electric field. This is justified as the interaction with the electric field is much stronger than the interactions with the magnetic field during the SFI field ramp. The SFI signal for different m_j states can then be calculated separately. The initial Rydberg states correspond to the Stark eigenstates in the combined magnetic and electric fields. The state $|r_1\rangle$ has sizable contributions only from the $m_j = -5/2 \dots 5/2$ substates of the $48D_{5/2}$ state, while the state $|r_2\rangle$ is given by a linear combination of zero-field states with different l and m_j values of the $n = 47$ manifold. The resulting signal is then given by the sum over individually calculated (interpolated for all l and m_j values) ion signals weighted by the initial population distribution.

APPENDIX E: CAVITY-DRIVEN RYDBERG TRANSITION

1. Steady-state Rydberg spectrum

We model the interaction of an atom on the Rydberg transition $|r_1\rangle \rightarrow |r_2\rangle$ with the MW field by a driven two-level system. With the Rabi frequency Ω , the decay rate Γ , and the resonant Rydberg transition frequency ω_{12} , the steady state population of $|r_2\rangle$ is [54]

$$\rho_{22} = \frac{|\Omega|^2/4}{(\omega_{\text{MW}} - \omega_{12})^2 + \Gamma^2/4 + |\Omega|^2/2}. \quad (\text{E1})$$

To account for the Rydberg transition linewidth, we assume that the transition frequencies are distributed according to a Gaussian function

$$S(\omega_{12}) \propto \exp\left[-\ln 2 \left(\frac{\omega_{12} - \bar{\omega}_{12}}{\Delta\omega_{12}/2}\right)^2\right], \quad (\text{E2})$$

where $\bar{\omega}_{12}$ is the mean transition frequency of the atoms in the resonant layer, and $\Delta\omega_{12}$ is the full width at half maximum. The appropriately weighted Rydberg state population is then

$$\tilde{\rho}_{22} = \int S(\omega_{12}) \rho_{22}(\omega_{12}) d\omega_{12}. \quad (\text{E3})$$

The atoms interact with the intracavity MW field with Rabi frequency $\Omega = dE_c/\hbar$, where E_c is given by Eq. (A1). We denote by $\bar{\Omega} \equiv \Omega(\omega_{\text{MW}} = \bar{\omega}_{12})$ the Rabi frequency of the injected MW field resonant with mean transition frequency $\bar{\omega}_{12}$ of the atoms in the resonant layer. We can then write

$$|\Omega(\omega_{\text{MW}})|^2 = |\bar{\Omega}|^2 \frac{(\bar{\omega}_{12} - \omega_c)^2 + \kappa^2/4}{(\omega_{\text{MW}} - \omega_c)^2 + \kappa^2/4}. \quad (\text{E4})$$

The combination of Eqs. (E1)–(E4) then yields the model function $p_2 = \frac{p}{1+a} \tilde{\rho}_{22} + p_0$ for the normalized ion counts p_2 which we use to fit the data in Fig. 4(b) with the offset p_0 , the amplitude $p/(1+a)$ and additional fitting parameters $\bar{\Omega}$, $\bar{\omega}_{12}$, and ω_c . From the fit we deduce $\bar{\omega}_{12} = 2\pi \times 20.5513$ GHz, $\omega_c = 2\pi \times 20.5495$ GHz, and $p/(1+a) \approx 0.2$.

2. Resonant Rabi oscillations

For a resonantly driven two-level atom, neglecting the population decay and coherence relaxation, the population difference between the states $|r_1\rangle$ and $|r_2\rangle$ is

$$D(\Omega, t) = \rho_{11} - \rho_{22} = \cos(\Omega t). \quad (\text{E5})$$

With the atomic cloud being laterally displaced by $x_0 \simeq 50 \mu\text{m}$ from the cavity center (see the inset in Fig. 4(c)), the MW field strength varies in the resonant atomic layer. We assume that the corresponding Rabi frequency varies approximately linearly in space,

$$\Omega(x) = \bar{\Omega} \left(1 + \frac{x - x_0}{\chi}\right). \quad (\text{E6})$$

The atomic density distribution in the layer is Gaussian, $n(x) \propto \frac{1}{\sqrt{2\pi}\sigma} \exp(-\frac{(x-x_0)^2}{2\sigma^2})$. The spatially averaged population difference is then

$$\bar{D}(t) = \int_{-\infty}^{\infty} n(x) D(\Omega(x), t) dx = e^{-\gamma^2 t^2} \cos(\bar{\Omega} t), \quad (\text{E7})$$

where $\gamma^2 = \frac{\sigma^2}{2\chi^2} \bar{\Omega}^2$. Hence, the spatial variation of the MW field leads to damping of the resonant Rabi oscillations, even if we neglect the decay and coherence relations of the atoms. From the MW field simulations, we estimate the relative change of the Rabi frequency across the cloud of width $\sigma = 25 \mu\text{m}$ to be $b = \sigma/\chi \lesssim 0.3$, consistent with the observations in Fig. 4(c), where we have $\gamma_{\text{fit}} = 1.6 \pm 0.2 \mu\text{s}^{-1}$, $2.7 \pm 0.6 \mu\text{s}^{-1}$, and $7.5 \pm 1.3 \mu\text{s}^{-1}$ for $\Omega_{\text{fit}} = 2\pi \times 1.7 \pm 0.1$ MHz, $\Omega_{\text{fit}} = 2\pi \times 4.3 \pm 0.2$ MHz and $\Omega_{\text{fit}} = 2\pi \times 7.7 \pm 0.3$ MHz, respectively. We estimate that the small deviation from the scaling $\Omega \propto \sqrt{P}$ is mainly due to small drifts in the cavity temperature leading to slight variations of the MW field strength on the timescale of hours.

- [1] Z.-L. Xiang, S. Ashhab, J. You, and F. Nori, Hybrid quantum circuits: Superconducting circuits interacting with other quantum systems, *Rev. Mod. Phys.* **85**, 623 (2013).
 [2] G. Kurizki *et al.*, Quantum technologies with hybrid systems, *Proc. Natl. Acad. Sci. USA* **112**, 3866 (2015).

- [3] A. A. Clerk, K. W. Lehnert, P. Bertel, J. R. Petta, and Y. Nakamura, Hybrid quantum systems with circuit quantum electrodynamics, *Nat. Phys.* **16**, 257 (2020).
 [4] R. J. Schoelkopf and S. M. Girvin, Wiring up quantum systems, *Nature (London)* **451**, 664 (2008).

- [5] M. H. Devoret and R. J. Schoelkopf, Superconducting circuits for quantum information: An outlook, *Science* **339**, 1169 (2013).
- [6] A. I. Lvovsky, B. C. Sanders and W. Tittel, Optical quantum memory, *Nat. Photonics* **3**, 706 (2009).
- [7] M. Fleischhauer, A. Imamoglu and J. P. Marangos, Electromagnetically induced transparency: Optics in coherent media, *Rev. Mod. Phys.* **77**, 633 (2005).
- [8] K. Hammerer, A. S. Sørensen, and E. S. Polzik, Quantum interface between light and atomic ensembles, *Rev. Mod. Phys.* **82**, 1041 (2010).
- [9] A. Blais, R.-S. Huang, A. Wallraff, S. M. Girvin and R. J. Schoelkopf, Cavity quantum electrodynamics for superconducting electrical circuits: An architecture for quantum computation, *Phys. Rev. A* **69**, 062320 (2004).
- [10] X. Zhu *et al.*, Coherent coupling of a superconducting flux qubit to an electron spin ensemble in diamond, *Nature (London)* **478**, 221 (2011).
- [11] Y. Kubo, C. Grezes, A. Dewes, T. Umeda, J. Isoya, H. Sumiya, N. Morishita, H. Abe, S. Onoda, T. Ohshima, V. Jacques, A. Dreau, J. F. Roch, I. Diniz, A. Auffeves, D. Vion, D. Esteve, and P. Bertet, Hybrid Quantum Circuit with a Superconducting Qubit Coupled to a Spin Ensemble, *Phys. Rev. Lett.* **107**, 220501 (2011).
- [12] S. Saito, X. Zhu, R. Amsuss, Y. Matsuzaki, K. Kakuyanagi, T. Shimo-Oka, N. Mizuochi, K. Nemoto, W. J. Munro, and K. Semba, Towards Realizing a Quantum Memory for a Superconducting Qubit: Storage and Retrieval of Quantum States, *Phys. Rev. Lett.* **111**, 107008 (2013).
- [13] P. Treutlein, P. Hommelhoff, T. Steinmetz, T. W. Hänsch, and J. Reichel, Coherence in Microchip Traps, *Phys. Rev. Lett.* **92**, 203005 (2004).
- [14] J. Fortágh and C. Zimmermann, Magnetic microtraps for ultracold atoms, *Rev. Mod. Phys.* **79**, 235 (2007).
- [15] C. Roux *et al.*, Bose-Einstein condensation on a superconducting atom chip, *Europhys. Lett.* **81**, 56004 (2008).
- [16] C. Hermann-Avigliano, R. C. Teixeira, T. L. Nguyen, T. Cantat-Moltrecht, I. Dotsenko, S. Gleyzes, J. M. Raimond, S. Haroche, and M. Brune, Long coherence times for Rydberg qubits on a superconducting atom chip, *Phys. Rev. A* **90**, 040502(R) (2014).
- [17] S. Bernon *et al.*, Manipulation and coherence of ultra-cold atoms on a superconducting atom chip, *Nat. Commun.* **4**, 2380 (2013).
- [18] P. Rabl, D. DeMille, J. M. Doyle, M. D. Lukin, R. J. Schoelkopf, and P. Zoller, Hybrid Quantum Processors: Molecular Ensembles as Quantum Memory for Solid State Circuits, *Phys. Rev. Lett.* **97**, 033003 (2006).
- [19] J. Verdú, H. Zoubi, C. Koller, J. Majer, H. Ritsch, and J. Schmiedmayer, Strong Magnetic Coupling of an Ultracold Gas to a Superconducting Waveguide Cavity, *Phys. Rev. Lett.* **103**, 043603 (2009).
- [20] K. R. Patton and U. R. Fischer, Ultrafast Quantum Random Access Memory Utilizing Single Rydberg Atoms in a Bose-Einstein Condensate, *Phys. Rev. Lett.* **111**, 240504 (2013).
- [21] J. de Hond, R. vanBijnen, S. J. J. M. F. Kokkelmans, R. J. C. Spreeuw, H. B. van Linden van den Heuvell, and N. J. van Druten, From coherent collective excitation to Rydberg blockade on an atom chip, *Phys. Rev. A* **98**, 062714 (2018).
- [22] D. Petrosyan, K. Mølmer, J. Fortágh, M. Saffman, Microwave to optical conversion with atoms on a superconducting chip, *New J. Phys.* **21**, 073033 (2019).
- [23] H. Hattermann *et al.*, Coupling ultracold atoms to a superconducting coplanar waveguide resonator, *Nat. Commun.* **8**, 2254 (2017).
- [24] A. S. Sørensen, C. H. van der Wal, L. I. Childress and M. D. Lukin, Capacitive Coupling of Atomic Systems to Mesoscopic Conductors, *Phys. Rev. Lett.* **92**, 063601 (2004).
- [25] D. Petrosyan and M. Fleischhauer, Quantum Information Processing with Single Photons and Atomic Ensembles in Microwave Coplanar Waveguide Resonators, *Phys. Rev. Lett.* **100**, 170501 (2008).
- [26] D. Petrosyan, G. Bensky, G. Kurizki, I. Mazets, J. Majer, and J. Schmiedmayer, Reversible state transfer between superconducting qubits and atomic ensembles, *Phys. Rev. A* **79**, 040304(R) (2009).
- [27] S. D. Hogan, J. A. Agner, F. Merkt, T. Thiele, S. Filipp, and A. Wallraff, Driving Rydberg-Rydberg Transitions from a Coplanar Microwave Waveguide, *Phys. Rev. Lett.* **108**, 063004 (2012).
- [28] S. Haroche, Nobel lecture: Controlling photons in a box and exploring the quantum to classical boundary, *Rev. Mod. Phys.* **85**, 1083 (2013).
- [29] A. Morgan and S. Hogan, Coupling Rydberg Atoms to Microwave Fields in a Superconducting Coplanar Waveguide Resonator, *Phys. Rev. Lett.* **124**, 193604 (2020).
- [30] B. T. Gard, K. Jacobs, R. McDermott and M. Saffman, Microwave-to-optical frequency conversion using a cesium atom coupled to a superconducting resonator, *Phys. Rev. A* **96**, 013833 (2017).
- [31] J. P. Covey, A. Sipahigil and M. Saffman, Microwave-to-optical conversion via four-wave mixing in a cold ytterbium ensemble, *Phys. Rev. A* **100**, 012307 (2019).
- [32] J. D. Pritchard, J. A. Isaacs, M. A. Beck, R. McDermott and M. Saffman, Hybrid atom-photon quantum gate in a superconducting microwave resonator, *Phys. Rev. A* **89**, 010301(R) (2014).
- [33] L. Sárkány, J. Fortágh, and D. Petrosyan, Long-range quantum gate via Rydberg states of atoms in a thermal microwave cavity, *Phys. Rev. A* **92**, 030303(R) (2015).
- [34] L. Sárkány, J. Fortágh, and D. Petrosyan, Faithful state transfer between two-level systems via an actively cooled finite-temperature cavity, *Phys. Rev. A* **97**, 032341 (2018).
- [35] L. Tian, P. Rabl, R. Blatt and P. Zoller, Interfacing Quantum-Optical and Solid-State Qubits, *Phys. Rev. Lett.* **92**, 247902 (2004).
- [36] D. Bothner, D. Wiedmaier, B. Ferdinand, R. Kleiner, and D. Koelle, Improving Superconducting Resonators in Magnetic Fields by Reduced Field Focussing and Engineered Flux Screening, *Phys. Rev. Appl.* **8**, 034025 (2017).
- [37] D. Bothner *et al.*, Inductively coupled superconducting half wavelength resonators as persistent current traps for ultracold atoms, *New J. Phys.* **15**, 093024 (2013).
- [38] A. Tauschinsky, R. M. T. Thijssen, S. Whitlock, H. B. van Linden van den Heuvell, and R. J. C. Spreeuw, Spatially resolved excitation of Rydberg atoms and surface effects on an atom chip, *Phys. Rev. A* **81**, 063411 (2010).
- [39] H. Hattermann, M. Mack, F. Karlewski, F. Jessen, D. Cano, and J. Fortágh, Detrimental adsorbate fields in experiments with

- cold Rydberg gases near surfaces, *Phys. Rev. A* **86**, 022511 (2012).
- [40] K. Chan, M. Siercke, C. Hufnagel and R. Dumke, Adsorbate Electric Fields on a Cryogenic Atom Chip, *Phys. Rev. Lett.* **112**, 026101 (2014).
- [41] J. Sedlacek, E. Kim, S. T. Rittenhouse, P. F. Weck, H. R. Sadeghpour, and J. P. Shaffer, Electric Field Cancellation on Quartz by Rb Adsorbate-Induced Negative Electron Affinity, *Phys. Rev. Lett.* **116**, 133201 (2016).
- [42] M. L. Zimmerman, M. G. Littman, M. M. Kash and D. Kleppner, Stark structure of the Rydberg states of alkali-metal atoms, *Phys. Rev. A* **20**, 2251 (1979).
- [43] J. Grimm *et al.*, Measurement and numerical calculation of rubidium Rydberg Stark spectra, *New J. Phys.* **17**, 053005 (2015).
- [44] A. Stibor, S. Kraft, T. Campey, D. Komma, A. Gunther, J. Fortágh, C. J. Vale, H. Rubinsztein-Dunlop, and C. Zimmermann, Calibration of a single-atom detector for atomic microchips, *Phys. Rev. A* **76**, 033614 (2007).
- [45] A. Günther, H. Bender, A. Stibor, J. Fortágh, C. Zimmermann, Observing quantum gases in real time: Single-atom detection on a chip, *Phys. Rev. A* **80**, 011604(R) (2009).
- [46] V. C. Gregoric, X. Kang, Z. C. Liu, Z. A. Rowley, T. J. Carroll, and M. W. Noel, Quantum control via a genetic algorithm of the field ionization pathway of a Rydberg electron, *Phys. Rev. A* **96**, 023403 (2017).
- [47] A. Gürtler and W. van der Zande, ℓ -state selective field ionization of rubidium Rydberg states, *Phys. Lett. A* **324**, 315 (2004).
- [48] T. F. Gallagher, *Rydberg Atoms* (Cambridge University Press, Cambridge, 2005).
- [49] M. Mack, J. Grimm, F. Karlewski, L. Sárkány, H. Hattermann, and J. Fortágh, All-optical measurement of Rydberg-state lifetimes, *Phys. Rev. A* **92**, 012517 (2015).
- [50] I. Beterov, I. Ryabtsev, D. Tretyakov and V. Entin, Quasiclassical calculations of blackbody-radiation-induced depopulation rates and effective lifetimes of Rydberg ns , np , and nd alkali-metal atoms with $n \leq 80$, *Phys. Rev. A* **79**, 052504 (2009).
- [51] M. Peper, J. Deiglmayr, F. Merkt, C. Sanna and H. V. L. van den Heuvell, Magic Rydberg-Rydberg transitions in electric fields, *Phys. Rev. A* **100**, 032512 (2019).
- [52] A. Megrant *et al.*, Planar superconducting resonators with internal quality factors above one million, *Appl. Phys. Lett.* **100**, 113510 (2012).
- [53] J. Grimm, M. Stecker, M. Kaiser, F. Karlewski, L. Torralbo-Campo, A. Gunther, and J. Fortágh, Ionization spectra of highly Stark-shifted rubidium Rydberg states, *Phys. Rev. A* **96**, 013427 (2017).
- [54] P. Lambropoulos and D. Petrosyan, *Fundamentals of Quantum Optics and Quantum Information* (Springer, Berlin, 2007).